Nano Research

Open Access

Research Article

Ferrocene conjugated glutathione consumption for enhanced ferroptosis therapy and chemotherapy

Limei Zhang[1,§], Huatai Zhu[1,§], Yuting Ren[1], Peng Ye[1], and Jiandu Lei[1,2] ✉

[1] *Beijing Key Laboratory of Lignocellulosic Chemistry, Beijing Forestry University, Beijing 100083, China*
[2] *MOE Engineering Research Center of Forestry Biomass Materials and Bioenergy, Beijing Forestry University, Beijing 100083, China*
[§] *Limei Zhang and Huatai Zhu contributed equally to this work.*

Cite this article: *Nano Research*, **2025**, *18*, 94907298. https://doi.org/10.26599/NR.2025.94907298

ABSTRACT: As the backbone of tumor therapy, chemotherapy is prone to tumor resistance due to its apoptotic pathway. Ferroptosis, as an effective form of non-apoptotic cell death, can overcome chemotherapy apoptosis-induced resistance. Therefore, the combination of chemotherapy and ferroptosis is a highly promising tumor treatment strategy. However, high glutathione (GSH) and insufficient intracellular iron content in the tumor environment limit the efficiency of ferroptosis-mediated anticancer. Not only that, simultaneous intracellular delivery of iron sources, ferroptosis inducers, and chemotherapeutic agents remains a major challenge. Here, we constructed a self-assembled nano prodrug system to co-deliver iron sources, ferroptosis inducers, and anti-cancer drugs for combined ferroptosis and chemotherapy. In the tumor microenvironment, high levels of GSH triggered redox-responsive disulfide bonding, which induced the disassembly of this nano prodrug system (PFSH@HCPT), releasing hydroxycamptothecin (HCPT), honokiol (HNK) and ferrocene (Fc). HCPT induced cell death via apoptosis and Fc triggered the Fenton reaction, which induced ferroptosis. HNK inhibited the activity of glutathione peroxidase 4 (GPX4) to enhance ferroptosis, and on the other hand, it further induced cell death via apoptosis. Meanwhile, the combined strategy of HNK-mediated resistance and ferroptosis-induced resistance mechanism further overcame the resistance of HCPT and significantly improved the therapeutic efficacy. This nano prodrug system realized the "multi-machine integrated" therapeutic efficacy and showed great therapeutic potential, which may open up a new way for effective cancer treatment.

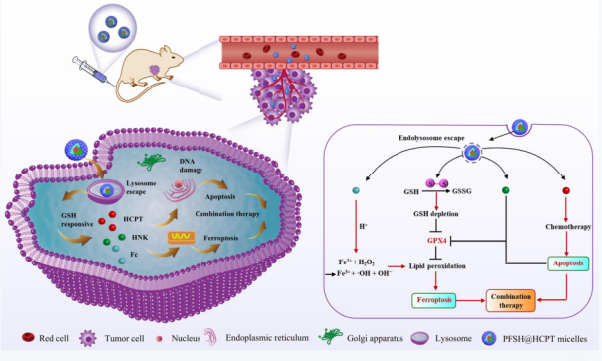

KEYWORDS: ferroptosis, glutathione consumption, ferrocene (Fc), honokiol (HNK), hydroxycamptothecin (HCPT)

1 Introduction

Colorectal cancer, the third most common cancer in the world, has a high incidence and mortality rate [1–3]. Although chemotherapy is still the current pillar of treatment for colorectal cancer due to its good tumour killing ability [4], this single chemotherapeutic approach can only temporarily alleviate the cancer [5] and is prone to chemoresistance and side effects [6, 7]. Therefore, multiple therapeutic combination strategies or avoidance of apoptosis-induced chemoresistance are highly promising strategies for exploring colorectal cancer treatment.

In recent years, it has been shown that ferroptosis can overcome chemotherapeutic apoptosis-induced resistance [8–11], and thus the combination of apoptosis and ferroptosis shows great potential in addressing tumor heterogeneity-induced drug resistance. Ferroptosis, a novel form of iron-regulated programmed cell death, results from iron-dependent accumulation of lipid peroxides [12–14]. One of the reasons for its emergence as a potential target for cancer therapy is its potency in removing drug-resistant tumour cells and highly metastatic tumour cells undergoing epithelial-mesenchymal transition [15–17]. Whereas, recurrence and metastasis remain the leading causes of tumour-related deaths in colorectal cancer patients [18, 19]. Therefore, the combination of apoptosis and ferroptosis is expected to be an effective strategy for the treatment of colorectal cancer. However, high glutathione (GSH) and insufficient intracellular iron content in the tumor environment limit the efficiency of ferroptosis-mediated anticancer [20–23]. On-demand delivery of iron or modulation of iron metabolism has emerged as one of the alternative options to induce

Received: December 10, 2024; **Revised:** February 5, 2025
Accepted: February 10, 2025

✉Address correspondence to ljd2012@bjfu.edu.cn

ferroptosis. Even though there has been an ongoing effort to deliver ferrous iron with different nanocarriers to increase intracellular iron content to improve ferroptosis [24, 25]. However, the *in vivo* delivery of ferrous iron is challenging and still suffers from easy oxidation and poor drug-carrying efficiency [26, 27]. Therefore, ferrocene (Fc), as an effective divalent iron supplier coupled with its good chemical stability and biocompatibility [28, 29], shows great potential advantages in ferroptosis studies.

Honokiol (HNK), an ferroptosis inducer, can induce ferroptosis in colon cancer cells by reducing glutathione peroxidase 4 (GPX4) activity [30]. In addition, it has been shown that HNK reverses P-gp-mediated multidrug resistance in tumors and synergistically sensitizes the antitumor activity of chemotherapeutic agents [31, 32]. Therefore, combination therapy by Fc and HNK has emerged as an effective strategy to develop iron source and intrastromal Schematic representation of nano prodrug micelles for eenhanced ferroptosis and chemotherapy. The amphiphilic polymer of coupled ferrocene and disulfide modified HNK (PFSH) was self-assembled into micelles loaded with the chemotherapeutic drug HCPT. The micelles disintegrated in the high GSH tumor microenvironment, releasing iron catalyst (Fc), anticancer drugs (HCPT, HNK), and GPX4 inhibitor (HNK) to achieve the combination of ferroptosis and chemotherapy and overcoming chemotherapeutic drug resistance through a dual-mechanism that significantly improved efficacy ferroptosis. It not only enhances the sensitivity of cancer cells to ferroptosis, but the synergistic mechanisms of HNK reversal of P-gp-mediated multidrug resistance in tumors and induction of ferroptosis to overcome chemotherapeutic apoptosis-induced resistance further overcame chemotherapeutic drug resistance and enhanced antitumor activity. However, the poor water solubility and low targeting ability of these small molecules greatly limit their *in vivo* application [33, 34]. Effective delivery of drugs to tumour cells using nano prodrug system remains a favourable means to increase efficiency and reduce toxicity [35]. Among them, smart-responsive prodrug system has become a mainstream research direction for drug delivery [36]. Therefore, designing a nano prodrug system for co-delivery of iron sources, ferroptosis inducers and chemotherapeutic drugs remains a major challenge.

Herein, as a proof of concept, we developed a nano prodrug system to co-deliver iron source (Fc), ferroptosis inducer (HNK), and anticancer drug (HNK, 10-hydroxycamptothecin (HCPT)) for combined ferroptosis and chemotherapy, as shown in Fig. 1. Fc was linked to an eight-arm polyethylene glycol (NH_2-PEG-Fc), which was then coupled to HNK via a GSH-reactive trigger (disulfide bond) to self-assemble to form nanoparticles (PFSH). HCPT was co-loaded into PFSH to further self-assemble to form nanoparticles (PFSH@HCPT). High levels of GSH triggered disulfide bonding and induced disassembly of PFSH@HCPT, releasing HCPT, HNK, and Fc. HCPT induced cell death via apoptosis and Fc triggered the Fenton reaction, inducing ferroptosis. HNK inhibited GPX4 activity to enhance ferroptosis on the one hand, and further induced cell death via apoptosis on the other hand. Meanwhile, the combined strategy of HNK-mediated resistance and ferroptosis induced resistance mechanism further overcame the resistance of HCPT and significantly improved the therapeutic efficacy. This nano system achieved the efficacy of "multi-machine integrated" and may provide new insights into more effective anti-colon cancer treatments.

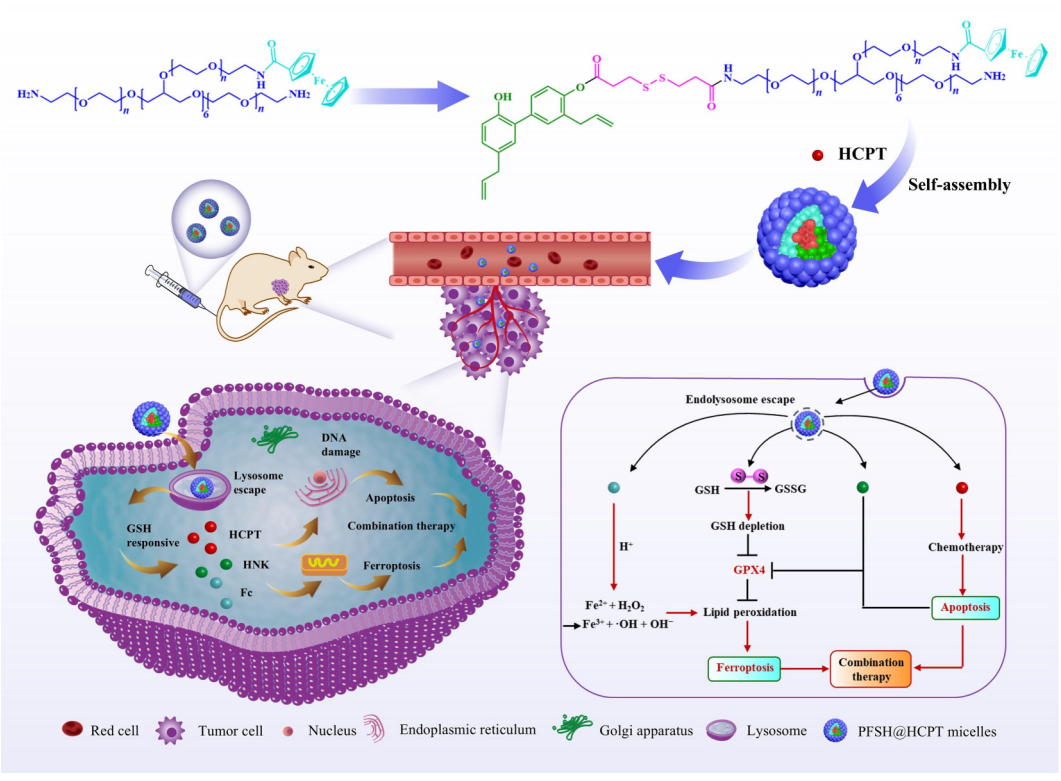

Figure 1 Schematic representation of nano prodrug micelles for eenhanced ferroptosis and chemotherapy. The amphiphilic polymer of coupled ferrocene and disulfide modified HNK (PFSH) was self-assembled into micelles loaded with the chemotherapeutic drug HCPT. The micelles disintegrated in the high GSH tumor microenvironment, releasing iron catalyst (Fc), anticancer drugs (HCPT, HNK), and GPX4 inhibitor (HNK) to achieve the combination of ferroptosis and chemotherapy and overcoming chemotherapeutic drug resistance through a dual-mechanism that significantly improved efficacy.

2 Materials and methods

2.1 Materials

8arm-poly(ethylene glycol)-amine (8armPEG-NH_2, 40,000 Da) was sourced by Ponsure Biotechnology Ltd. HNK, N-hydroxy succinimide (NHS), tris-(2-carboxyethyl)-phosphine hydrochloride (TCEP-HCl), sodium dodecyl sulfate (SDS), oxalyl chloride, pyridine, tetrahydrofuran (THF), N,N-dimethylformamide (DMF), p-phthalic acid (TA), methylene blue (MB), 1,10-phenanthroline and coumarin 6 (C6) were purchased from Shanghai Macklin Biochemical Co., Ltd. 3,3'-Disulfanediyldipropanoic acid (DPA), ferrocenecarboxylic acid (Fc-COOH) and hydrogen peroxide (H_2O_2) were obtained from Shanghai Aladdin Biochemical Technology Co., Ltd. 1-(3-Dimethylaminopropyl)-3-ethylcarbodiimide (EDC) was provided from Beijing Solarbio Technology Co., Ltd. 10-Hydroxycamptothecin (HCPT) was from Chengdu Pufei De Biotech Co., Ltd. All the other solvents used in the study were purchased from Modern Oriental Fine Chemistry Technology Co., Ltd.

DMEM medium, RPMI 1640 medium, fetal bovine serum (FBS), trypsin (0.25% in HBSS) and penicillin–streptomycin were obtained from Shanghai Da Te Xi Er Biotechnology Co., Ltd. Cell-Counting Kit-8 (CCK-8) was achieved from Beyotime Biotechnology Co., Ltd. Hoechst 33258 was from Beijing Solarbio Technology Co., Ltd. 4% paraformaldehyde fix solution was provided from Shanghai yuan ye Bio-Technology Co., Ltd. 2',7'-Dichlorofluorescin diacetate (DCFH-DA) was purchased from Bide Pharmatech Ltd. Malonaldehyde (MDA) detection assay kit and GSH detection assay kit were obtained from Beyotime Biotechnology Co. Ltd. (Shanghai, China).

2.2 Synthesis of copolymer

2.2.1 *Synthesis of NH_2-PEG-Fc*

NH_2-PEG-Fc was synthesized by reference to the typical amidation method (Scheme S1 in the Electronic Supplementary Material (ESM)). Ferrocenecarboxylic acid (4.6 mg, 20 μmol), EDC (4.8 mg, 25 μmol) and NHS (4.4 mg, 37.5 μmol) reacted in anhydrous dimethyl sulfoxide (DMSO) at room temperature for 4 h to activate the carboxyl groups. Then, 8armPEG-NH_2 (200 mg, 5 μmol) in anhydrous DMSO was added dropwise in the mixture for stirring 48 h at room temperature. The mixture was purified by dialysis (MWCO 20,000 Da) with ethanol for 24 h, followed by spin-drying (yield: 84.5%). The products were characterized by a Bruker Avance III HD 500MHz proton nuclear magnetic resonance spectrometer (^{1}H NMR), an ALPHA Fourier transform infrared spectrometer (KBr method) and an N 5000 ultraviolet–visible spectrometer.

2.2.2 *Synthesis of HNK-SS-COOH*

The synthesis of HNK-SS-COOH was carried out according to the reported method (Scheme S1 in the ESM) [37]. DPA (210.3 mg, 1 mmol) and catalyst amount of DMF (40 μL) were mixed in 10 mL anhydrous THF. The reaction was maintained at 0 °C, followed by adding oxalyl chloride (105 μL, 1.23 mmol) dropwise at 0 °C to react at room temperature for 3 h. HNK (266.4 mg, 1 mmol) and anhydrous pyridine (0.81 mL, 10 mmol) were mixed in 10 mL anhydrous THF. Next, DPA was attached to HNK by mixing and reacting at room temperature with light protection for 5 h. After the solvent of the mixture solution was removed, the product to be purified was dissolved in dichloromethane (DCM) and extracted 3 times with 0.1 mM hydrochloric acid solution. Afterwards, the organic phase was collected and DCM was removed by rotary evaporation. Then, HNK-SS-COOH was purified by silica gel column chromatography eluted with DCM/methanol (100:1, v/v), followed by spin-drying (yield: 40.8%). The products were also analyzed using the same characterization methods described above. In addition, the structure of the products was performed by triple quadrupole mass spectrometry (Agilent 1290-6470).

2.2.3 *Synthesis of copolymer PEG-Fc-SS-HNK*

The conjugation of HNK-SS-COOH to the polymer backbone (NH_2-PEG-Fc) was achieved by the classical amidation reaction (Scheme S1 in the ESM). Briefly, HNK-SS-COOH (105.8 mg, 0.2 mmol), EDC (76.7 mg, 0.2 mmol) and NHS (69.1 mg, 0.3 mmol) were mixed in anhydrous DMSO and the reaction was maintained at room temperature for 4 h. Next, NH_2-PEG-Fc (100 mg, 25 μmol) in anhydrous DMSO was added dropwise to the mixture for stirring 48 h at room temperature. Then, the mixture was purified by dialysis (MWCO 20,000 Da) with DMSO and ethanol for 48 h, followed by spin-drying (yield: 89.1%). The products were also analyzed using the same characterization methods as in Section 2.2.1.

2.3 Micelles manufacture and characterization

The self-assembly of amphiphilic PEG-Fc-SS-HNK conjugates employed the nanoprecipitation method [10]. PEG-Fc-SS-HNK (20 mg) in 1 mL DMSO was added to 10 mL deionized water dropwise, followed by stirring 3 h. Next, DMSO was removed by dialysis (MWCO 20,000 Da) and the micelles of PEG-Fc-SS-HNK (PFSH) were obtained through freeze-drying. The HCPT-loaded micelles were manufactured by the same method. Excess amounts of HCPT and PEG-Fc-SS-HNK were dissolved in DMSO and dialyzed with water, followed by centrifugation and freeze-drying, and the micelles of PEG-Fc-SS-HNK@HCPT (PFSH@HCPT) were obtained.

The hydrodynamic size and zeta potential of PFSH and PFSH@HCPT micelles (both 1 mg/mL) were characterized by Anton Paar Litesizer 500 (Anton Paar (Shanghai) Trading Co. Ltd). The kinetic stability of PFSH and PFSH@HCPT in phosphate buffered saline (PBS) was evaluated by monitoring the hydrodynamic particle size. The morphology of samples was determined by transmission electron microscope (HITACHI H-7650). Meanwhile, the content of micelle-loaded HCPT was determined using high-performance liquid chromatography (HPLC, Agilent 1200).

2.4 *In vitro* drug release

TCEP can rapidly break disulfide bonds and monitor the release of disulfide-bound drugs [38]. Therefore, the *in vitro* release of HNK and HCPT was evaluated by dialysis using PBS buffer containing 4% SDS with 10 mM TCEP as the release medium, which mimicked the tumor microenvironment [39]. The solution of PFSH@HCPT was placed in a dialysis bag (MWCO 3500 Da) immersed in the release medium, followed by shaking for 72 h at 37 °C. At specified time intervals, a quantity of sample solution was taken and an equal amount of the corresponding buffer was added. The content of HNK-SH and HCPT was detected by the HPLC method and the cumulative release rate was calculated. Fc can be transformed from hydrophobic to hydrophilic in an oxidizing

environment. In order to evaluate the effect of Fc on drug release, we examined the drug release behavior of micelles in the presence of 10 mM H_2O_2. The operation was performed as above.

2.5 The release of Fe^{2+} and ·OH generation

The absorption peak at 510 nm of the complex formed by the reaction of o-phenanthroline with Fe^{2+} was commonly used to indicate the concentration of Fe^{2+}. Fc-COOH (2 mM) and an equivalent amount of PFSH micelles were dispersed in acetic acid-sodium acetate buffer (0.2 M, pH 5.0) containing 1 mM H_2O_2, respectively. At the specified time, 400 μL reaction solution and 400 μL 0.15% o-phenanthroline solution were added to 3.6 mL acetic acid-sodium acetate buffer, and the absorbance at 510 nm was measured.

The ·OH generation of different samples was detected using the methylene blue photometric method, terephthalic acid fluorescence detection and electron spin resonance (ESR) analysis. Fc-COOH (0.1 mg/mL) and an equivalent amount of PFSH micelles were dispersed into the acetic acid-sodium acetate solution (9 mL) containing MB (15 μg/mL) respectively, followed by the addition of H_2O_2 (10 mM, 1 mL). The absorption spectra were recorded in the range of 500–750 nm. Fc-COOH (0.025 mg/mL) and an equivalent amount of PFSH micelles were added to 10 mL of acetic acid-sodium acetate solution containing TA (6 mM) and H_2O_2 (1 mM), and subsequently fluorescence emission spectra were recorded (Ex/Em: 310 nm/435 nm). ESR experiments were performed to determine hydroxyl radical production using 5,5-dimethyl-1-pyrroline N-oxide (DMPO) as a spin trap on an ESR instrument (Bruker EMXplus-6/1). To detect the DMPO-·OH signal, PFSH and PFSH@HCPT were dissolved in an aqueous solution of DMPO with a PFSH concentration of 1 mg/mL. The ESR spectra of the samples were recorded at room temperature.

2.6 Depletion of GSH

PFSH (7 mg/mL), DTNB (2 mM) and GSH (1 mM) were mixed in the acetic acid-sodium acetate solution and absorbance at 412 nm was recorded. The assay of micelle-free samples was used as a control.

2.7 *In vitro* cytotoxicity assay

L929 (NCTC clone 929) and CT26.WT (mouse colorectal carcinoma cells) were provided by Shanghai Jinyuan Biotechnology Co., Lt. The cells were inoculated in DMEM and RPMI medium 1640 containing 10% fetal bovine serum and 1% penicillin-streptomycin, respectively, and were kept at 37 °C with 5% CO_2. The cytotoxicity of samples was assessed using the standard CCK-8 assay. The corresponding cells (5×10^3 cells/well) were seeded in 96-well plates for 24 h, followed by incubating with different concentrations of the drugs for 24 h. Cell viability was then determined by recording the absorbance at 450 nm using an enzyme labeling instrument (Bio Tek Epoch).

2.8 Cellular uptake of micelles

C6 was loaded in micelles to confer fluorescent properties to the micelles for observing cellular uptake. CT26 cells (8×10^4 cells/well) were inoculated in 15 mm confocal dishes and incubated in 1640 medium at 37 °C for 24 h. Then the cells were incubated with fluorescent micelles (C6-equivalent concentration 5 μg/mL) for another 4 h. Next, the cells were washed with PBS, fixed with paraformaldehyde, washed with PBS and stained for nuclei by Hoechst 33342. The inverted fluorescence microscope (TE2000-S, Nikon) was utilized to observe cellular uptake.

To perform quantitative analysis, we adopted a flow cytometer (BD Accuri C6 Plus) to analyze cellular uptake. Cells were incubated with the samples, washed and resuspended in PBS for assay analysis.

2.9 Analysis of intracellular ROS levels

The intracellular ROS levels were analyzed with the fluorescent probe 2',7'-gichlorofluorescin diacetate (DCFH-DA). CT26 cells (8×10^4 cells/well) were incubated in confocal dishes for 24 h and treated with different samples for 4 h at the equivalent concentration on the next day. Subsequently, the cells were washed with PBS. The 20 μM DCFH-DA probe was added and incubated for 30 min away from light. Afterwards, the cells were washed with PBS and fixed by adding 4% paraformaldehyde, and the fluorescence was observed under an inverted fluorescence microscope.

2.10 Intracellular GSH levels and lipid peroxidation detection

The intracellular GSH levels and lipid hydroperoxides (LPOs) were evaluated by the GSH assay kit (Beijing Solarbio Science & Technology Co., Ltd, BC1175) and Lipid Peroxidation (MDA) assay kit (Beijing Solarbio Science & Technology Co., Ltd, BC0025), respectively. CT26 cells (5×10^4 cells/well) were inoculated into 6-well plates and cultured for 24 h. Then, equivalent concentrations of different samples were added and cultured for 24 h. Cells were collected and lysed with lysis buffer, and the supernatants were assayed for quantification of GSH and MDA using the appropriate kits.

2.11 Hemolysis assay

In vitro determination of hemolytic properties is an important method for evaluating the hemocompatibility of drugs, which is measured by a standard hemolysis test. The erythrocyte suspension (0.5 mL) was mixed with PFSH micelles (HNK 25 μg/mL), PFSH@HCPT micelles (HCPT 25 μg/mL), saline (negative control) and ultrapure water (positive control) (0.5 mL), respectively. They were incubated at 37 °C for 3 h, then centrifuged and the absorbance of the supernatant at 540 nm was recorded.

2.12 *In vivo* efficacy assessment

All animal experiments were conducted in accordance with the relevant policies of the Experimental Animal Welfare and Ethics Committee of Beijing. BALB/c female mice (4–6 weeks, 18–20 g) were obtained from Beijing Vital River Laboratory Animal Technology Co., Ltd. CT26 cell suspension (100 μL, 1×10^6 cells/each, PBS) was subcutaneously inoculated into mice on the right side to establish a tumor-bearing model. After 6 days, the mice were randomly divided into 5 groups (n = 5). HNK, HCPT, PFSH, PFSH@HCPT and PBS (10 mg/kg for HNK and HCPT dose per mouse) were injected intravenously every three days during the whole treatment. Tumor volumes and mouse body weights were recorded every two days after administration. At the end of the efficacy study, the mice in each group were euthanized and the tumor tissues were collected for histological analysis by H&E staining.

2.13 *In vivo* bio-distribution

DiR-labeled micelles were first prepared as in Section 2.3. The tumor-bearing mice were divided into two groups (n = 3) and

given free DiR and DiR-loaded micelles (DiR dose of 0.5 mg/kg) by intravenous injection, respectively. The mice were anesthetized at different time points and DiR imaging was recorded with fluorescence imaging (IVIS Lumina).

2.14 Statistical analysis

Data were expressed as mean ± standard deviation. Significant differences were compared by one-way analysis of variance (ANOVA) or Student's t-test. Threshold *P*-values were considered significant at $^{*}P < 0.05$, $^{**}P < 0.01$, $^{***}P < 0.001$.

3 Results and discussion

3.1 Synthesis and characterization of copolymer

The synthetic route of NH_2-PEG-Fc and PEG-Fc-SS-HNK were illustrated in Scheme S1 in the ESM. The Fc-COOH was covalently linked to the partial amino group of PEG-NH_2 by controlling the feeding ratio to obtain the product of NH_2-PEG-Fc. Disulfide-bonded modified HNK was synthesized by the oxalyl chloride method and covalently linked to NH_2-PEG-Fc to get PEG-Fc-SS-HNK. The ^{1}H NMR spectra of Fc-COOH, 8armPEG-NH_2, and NH_2-PEG-Fc were shown in Fig. S1 in the ESM. The signals at 4.79 and 4.4 ppm were attributed to the protons of Fc, and the appearance of this characteristic peak in the spectra of NH_2-PEG-Fc suggested the successful linkage of Fc-COOH with 8armPEG-NH_2, that is NH_2-PEG-Fc. Figure S2 in the ESM showed the ^{1}H-NMR characterization of HNK, DPA and HNK-SS-COOH. The resonances at 6.85–7.25, 6.89–6.02 and 4.95–5.15 ppm were ascribed to the protons of HNK, indicating the successful linkage of HNK with DPA. The signals of the methylene peak adjacent to the disulfide bond appeared at 2.48 and 2.84 ppm. The ^{1}H NMR spectra of PEG-Fc-SS-HNK (PFSH) were illustrated in Fig. S3 in the ESM. The characteristic absorption peaks of HNK and Fc demonstrated the successful linkage of NH_2-PEG-FC with HNK-SS-COOH. FT-IR analysis was further performed to verify the structure of the copolymer. As shown in Fig. S4 in the ESM, the peak at 1652 cm^{-1} belonged to the characteristic absorption peak of Fc-COOH. The peak at 1652 cm^{-1} in the infrared absorption spectrum of NH_2-PEG-Fc was the peak from Fc-COOH and amide carbonyl stretching vibration, indicating its successful preparation. Similarly, as shown in Fig. S5 in the ESM, the peak at 1747 cm^{-1} in the infrared absorption spectrum of PEG-Fc-SS-HNK belonged to the characteristic absorption peak of HNK-SS-COOH, which proved the successful linkage of NH_2-PEG-FC with HNK-SS-COOH. The ultraviolet–visible (UV–Vis) spectroscopy and mass spectrometry results in the Figs. S6 and S7 in the ESM further confirmed the successful preparation of the samples. According to the ^{1}H NMR spectrum and UV spectrophotometry, the grafting rate of Fc was about 42.1%, and the rest of the branched chain was connected to the disulfide-modified HNK.

Subsequently, we employed a nanoprecipitation method to self-assemble amphiphilic PEG-Fc-SS-HNK to form nano micelles (PFSH) and obtained HCPT-loaded micelles, designating PEG-Fc-SS-HNK@HCPT (PFSH@HCPT). The hydrodynamic sizes of PFSH and PFSH@HCPT micelles were 83.1 ± 2.5 and 126.5 ± 2.1 nm, revealed by dynamic light scattering analysis (Fig. 2(a)). In addition, both micelles were negatively charged (Fig. 2(b)), giving them good cyclic stability. And PFSH and PFSH@HCPT exhibited good stability in PBS, which was shown in Fig. S8 in the ESM. Transmission electron microscopy (TEM) showed that the morphology of the two micelles was spherical (Figs. 2(d) and 2(e)), which indicated their self-assembly into stable nanoparticles. To investigate the redox-responsive behavior of PFSH, we examined the changes in particle size and morphology of nanoparticles under the action of 10 mM TCEP. The results, which were displayed in Figs. 2(c) and 2(f), showed that the PFSH was dissociated and the size became larger. The results were consistent with the literature description [40]. The drug loading of HCPT was determined to be 13.7% ± 0.2% by high-performance liquid chromatography (HPLC).

3.2 *In vitro* drug release

TCEP, as an alternative reducing agent to DTT, has an efficient disulfide bond-reducing power. Therefore, we chose TCEP as a reducing agent to evaluate the drug release behavior of micelles in a reducing environment. The concentration of the reducing agent was set at 10 mM to mimic the intracellular GSH concentration. As shown in Fig. 2(g), the comparison of the ^{1}H NMR spectra of HNK-SH and HNK-SS-COOH illustrated successful breakage of the disulfide bond. The characteristic peaks at 2.8 and 3.0 ppm were attributed to the characteristic methylene peak adjacent to the unreacted carboxyl terminus on the DPA. The characteristic peaks at 1.4 ppm were assigned to that of –SH. The disappearance of the characteristic peaks at 2.8 and 3.0 ppm and the appearance of the characteristic peaks at 1.4 ppm indicated the breakage of disulfide bonds. The structure of HNK-SH was further verified using mass spectrometry (Fig. S9 in the ESM). The release curve of HNK-SH (Fig. 2(h)) suggested that disulfide bonds were rapidly broken in the reducing environment. The release behavior of PFSH@HCPT in the reducing environment was faster than in the physiological environment, releasing approximately 94% of the drug. This release behavior was attributed to the fact that the disulfide-bonded HNK was connected to part of the branch chain and the other part of the branch chain was Fc, so the reducing environment was not sufficient to rapidly crack the nanoparticles. With the breakage of disulfide bonds, the equilibrium between hydrophilicity and hydrophobicity of nanoparticles was gradually broken, the particle size became larger, and the drug release was accelerated and increased. Due to the same reason, the shift from hydrophobicity to hydrophilicity of Fc due to oxidizing environment resulted in a slightly higher drug release, but there was no significant difference in the release curve from that of acidic conditions.

3.3 Extracellular ferroptosis efficacy

In addition to the release of HNK and HCPT in response to high levels of GSH, PFSH also released Fe^{2+} simultaneously in the tumor environment. Fe^{2+}, as an important iron source for inducing ferroptosis, accelerates the Fenton reaction to generate ·OH and induce ferroptosis. To explore this phenomenon, we assessed Fe^{2+} release and ·OH generation. The release of Fe^{2+} of PFSH micelles was determined by o-phenanthroline spectrophotometry. As shown in Fig. 3(a), PFSH could release Fe^{2+} in the presence of H_2O_2 to form complexes with phenanthroline and produce an absorption band at 510 nm. The slow release of Fe^{2+} was similar to the behavior of Fc-COOH. The rate of Fe^{2+} release from PFSH was slower compared to Fc-COOH (Fig. 3(b)). Similarly, TA and MB were used as probes to study the generation of ·OH. As shown in Fig. 3(c), both PFSH and Fc-COOH could degrade MB by generating ·OH through the Fenton reaction and Fc-COOH degraded MB better than PFSH, which was consistent with the result of Fe^{2+} release. By comparing the results shown in

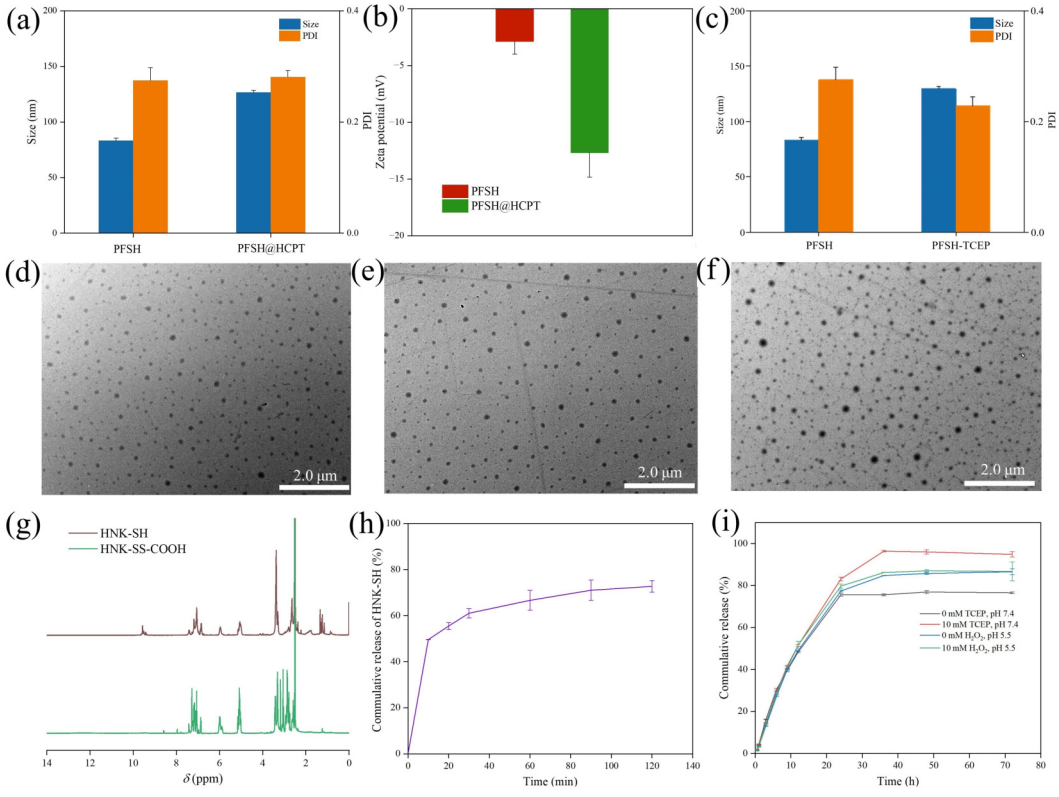

Figure 2 Characterization of PFSH and PFSH@HCPT nanodrugs. (a) Hydrodynamic size and polydispersity index (PDI), and (b) zeta potential of PFSH and PFSH@HCPT micelles. (c) DLS analysis of PFSH micelles with TCEP (10 mM). (d)–(f) TEM image of PFSH, PFSH@HCPT micelles and PFSH micelles with TCEP (10 mM). (g) ^{1}H NMR spectra of HNK-SS-COOH and HNK-SH. (h) *In vitro* release profile of HNK-SH from PFSH micelles with TCEP (10 mM) determined by HPLC. (i) *In vitro* release profiles of HCPT from PFSH micelles with different conditions for 72 h determined by HPLC.

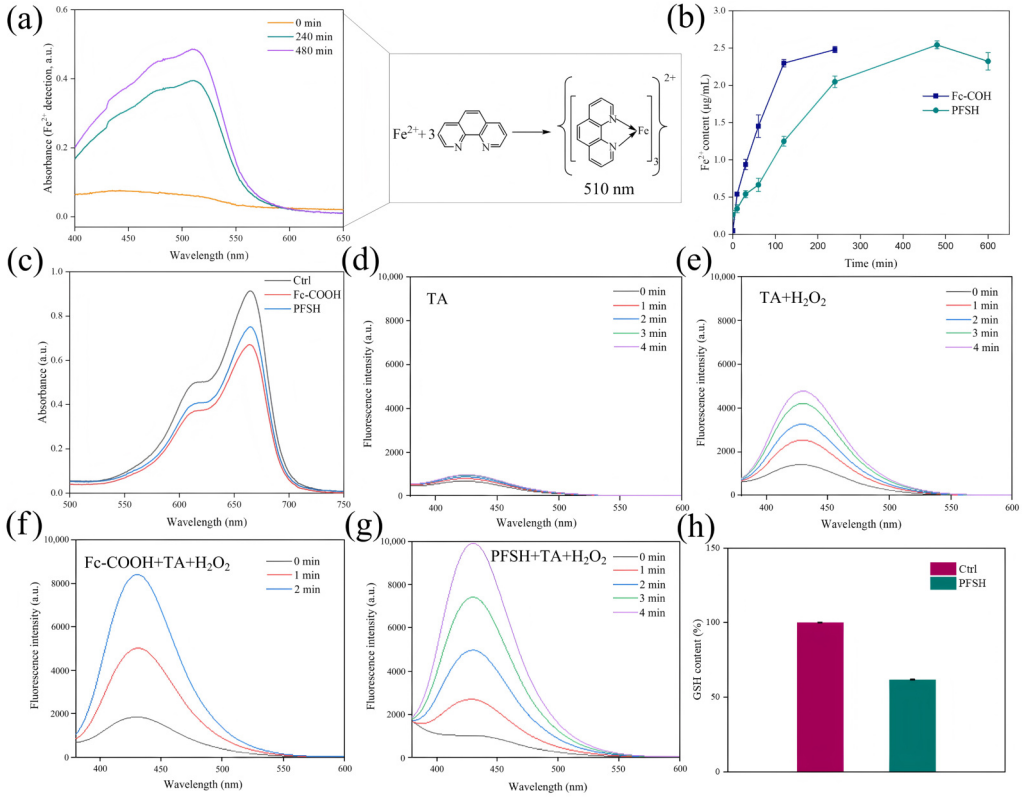

Figure 3 Extracellular ferroptosis efficacy of PFSH micelles. (a) UV–Vis absorption spectra of Fe^{2+} forming complexes with phenanthroline. (b) Release of Fe^{2+} from Fc-COOH and PFSH micelles. (c) Evaluation of the production of ·OH from methylene blue. (d)–(g) Assessment of ·OH production by terephthalic acid. (h) Depletion of GSH.

Figs. 3(d)–3(g), the Fe^{2+} released from PFSH and Fc-COOH catalyzed the Fenton reaction to promote the generation of ·OH. The production of ·OH was further verified by ESR (Fig. S10 in the ESM), which suggested that PFSH micelles and PFSH@HCPT micelles could induce the Fenton reaction to produce ·OH. The generation of ·OH and the breaking of disulfide bonds could consume more GSH (Fig. 3(h)), further inhibiting GPX4 activity and enhancing ferroptosis.

3.4 *In vitro* cytotoxicity

To evaluate the therapeutic effect of micelles *in vitro*, cell viability was investigated using the CCK-8 method. As shown in Fig. 4(a), after co-culture of different concentrations of HCPT and PFSH@HCPT with CT26 cells, the cell viability decreased significantly with the increase of the administered concentration, indicating that all of them had obvious killing effects on tumor cells. After different concentrations of HNK and PFSH were co-cultured with CT26 cells (Fig. 4(b)), the cell survival rate also decreased with the increase of the administered concentration, indicating that the HNK-containing group also had a certain killing effect on tumor cells. Notably, the toxic activity of PFSH@HCPT on L929 normal cells was reduced compared with that of free HCPT (Fig. 4(c)), which may be attributed to the fact that PFSH@HCPT had a certain passive targeting ability on tumor cells. The results were consistent with those reported in the literature [41]. As shown in Fig. 4(d), there was no significant difference in the toxic activity of different concentrations of HNK and PFSH on L929 normal cells.

3.5 Cellular uptake assay

To study the uptake behavior of CT26 cells towards nano micelles, we prepared C6-loaded nano micelles and observed their cellular uptake by inverted fluorescence microscopy. As shown in Fig. 5(a), there was no green fluorescence in the cells of the PFSH group alone, while the cells of the free C6 group and the PFSH@C6 group had obvious green fluorescence. The fluorescent micelles taken up by the cells were quantified by flow cytometry and the results were shown in Figs. 5(b) and 5(c). Th results indicated that PFSH@C6 could be effectively taken up by CT26 cells.

3.6 Intracellular ferroptosis efficacy

Inspired by the favorable properties of the nano micelles to generate ·OH *in vitro* , we further validated the generation of ·OH by NH_2-PEG-Fc (PEG-Fc) and PFSH in cancer cells using DCFH-DA. As shown in Figs. 6(a) and 6(b), the negligible green fluorescence of ROS was observed in the control group, whereas the strongest green fluorescence was observed in the PFSH group, suggesting that PFSH could generate high levels of ·OH. And the PFSH group exhibited a slightly higher fluorescence signal than the PEG-Fc group. Reducing GSH levels and downregulating GPX4 expression can induce ferroptosis. Therefore, we evaluated intracellular GSH levels after co-incubation of different drugs with cells. As shown in Fig. 6(c), HNK inhibited GPX4 expression, thereby reducing GSH levels. The Fc-containing nano micelles decreased GSH levels, with a more significant decrease in PFSH. This was owed to the fact that disulfide bonding could promote the oxidation of GSH to glutathione disulfide GSSG, which further down-regulated GPX4 expression. Meanwhile, the accumulation of intracellular LPOs induces ferroptosis. To assess the level of intracellular LPOs, we measured the content of their degradation product malondialdehyde (MDA), as shown in Fig. 6(d). The results indicated that Fc-containing nano micelles produced abundant LPOs, which effectively induced ferroptosis. These results were consistent with those of ROS generation, indicating that PFSH induced ferroptosis in cancer cells via LPOs.

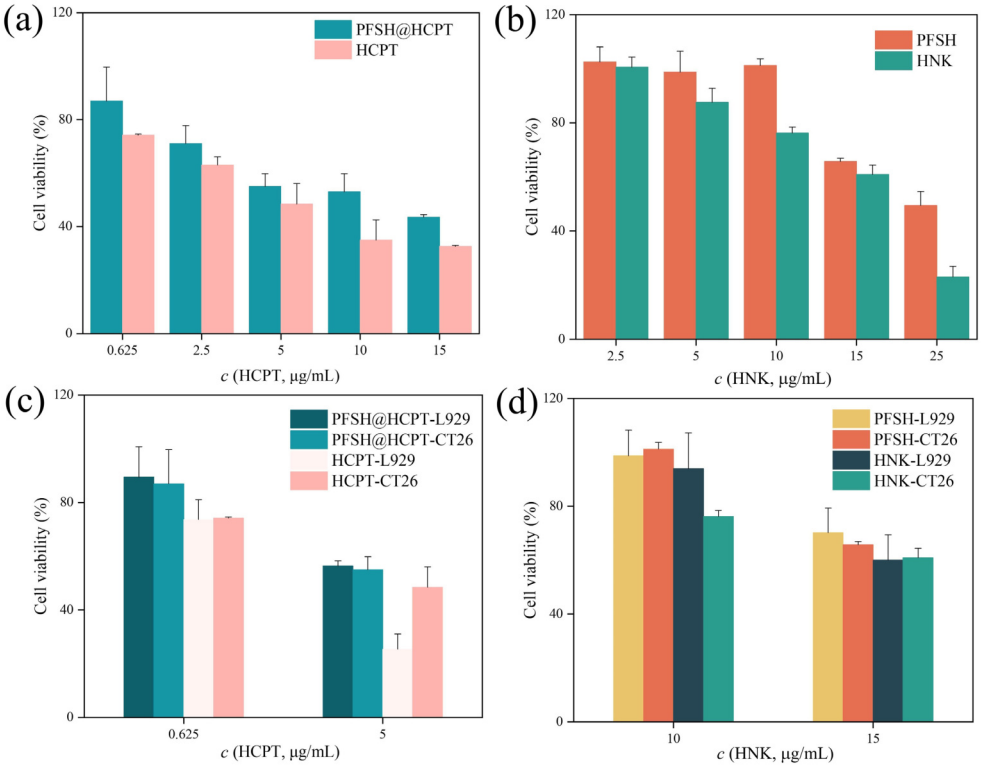

Figure 4 *In vitro* cytotoxicity analysis of nano-prodrugs. (a) and (b) Cell viability of CT26 cells with different formulations. (c) and (d) Cell viability of L929 cells with different formulations.

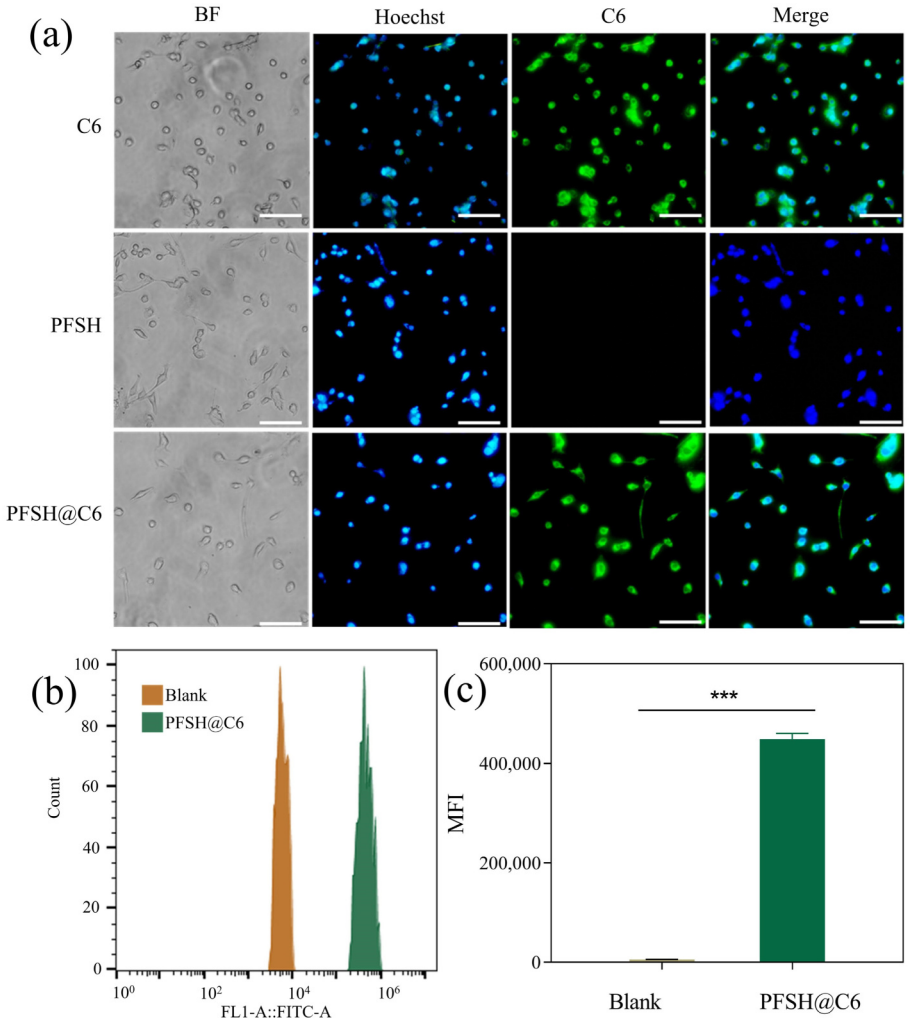

Figure 5 Cell uptake of nano-prodrugs in CT26 cells. (a) Representative inverted fluorescence microscopy images of CT26 cells incubated with the samples for 4 h. The scale bar represented 100 μm. (b) and (c) Fluorescence quantification by flow cytometry assay.

3.7 Hemocompatibility analysis

The hemolysis assay was further investigated to assess the biosafety of PFSH micelles and PFSH@HCPT micelles (Fig. S11 in the ESM). The hemolysis rates of the samples incubated with erythrocytes were less than 1.0%, suggesting that PFSH micelles and PFSH@HCPT micelles had high biosafety.

3.8 *In vivo* biodistribution and anticancer effects evaluation

Effective accumulation of nanoparticles at the tumor site is necessary to inhibit tumor proliferation and metastasis. To investigate the tumor accumulation behavior of PFSH in tumor-bearing mice, PFSH loaded with DiR (PFSH@DiR), was used to label the nanoparticles. As shown in Fig. 7(b), the PFSH@DiR group exhibited a strong fluorescence signal after 4 h of injection, indicating its effective accumulation and retention in tumor tissues, and obvious nanoparticle accumulation was still visible after 24 h, showing a long-lasting anti-tumor potential. In contrast, the free DiR group showed no obvious fluorescence signal at the tumor site. These results suggested that PFSH could be passively targeted to tumors and thus enriched in tumors.

As to investigate the anti-tumor effect of PFSH@HCPT *in vivo*, we established the CT26 tumor-bearing model. Mice were randomly divided into five groups (n = 5) and injected with PBS, HNK, HCPT, PFSH and PFSH@HCPT every 3 days, and the tumor volume and body weight of the mice were monitored throughout the treatment period (Figs. 7(c) and 7(d)). As shown in Fig. 7(c), compared with the control group (PBS group), the free HNK group showed some therapeutic efficacy whereas the PFSH group significantly suppressed tumors. The most significant tumor suppression effect was observed in the PFSH@HCPT group, suggesting that the ferroptosis treatment together with chemotherapy enhanced the anticancer effect. In addition, the body weights of mice in all groups displayed no significant changes during the treatment period (Fig. 7(d)), indicating that HNK, PFSH and PFSH@HCPT used during the treatment period showed little toxicity, whereas the HCPT group exhibited body weight loss, which illustrated its slight adverse effects *in vivo*. In addition, histopathological analysis of tumors in each group was performed by H&E staining to assess the antitumor effect (Fig. 7(e)). The PFSH@HCPT group exhibited greater histologic damage compared to the other groups. The above results confirmed that PFSH@HCPT nanoparticles enhanced the effects of ferroptosis therapy and chemotherapeutic action, demonstrating a stronger anti-tumor therapeutic potential.

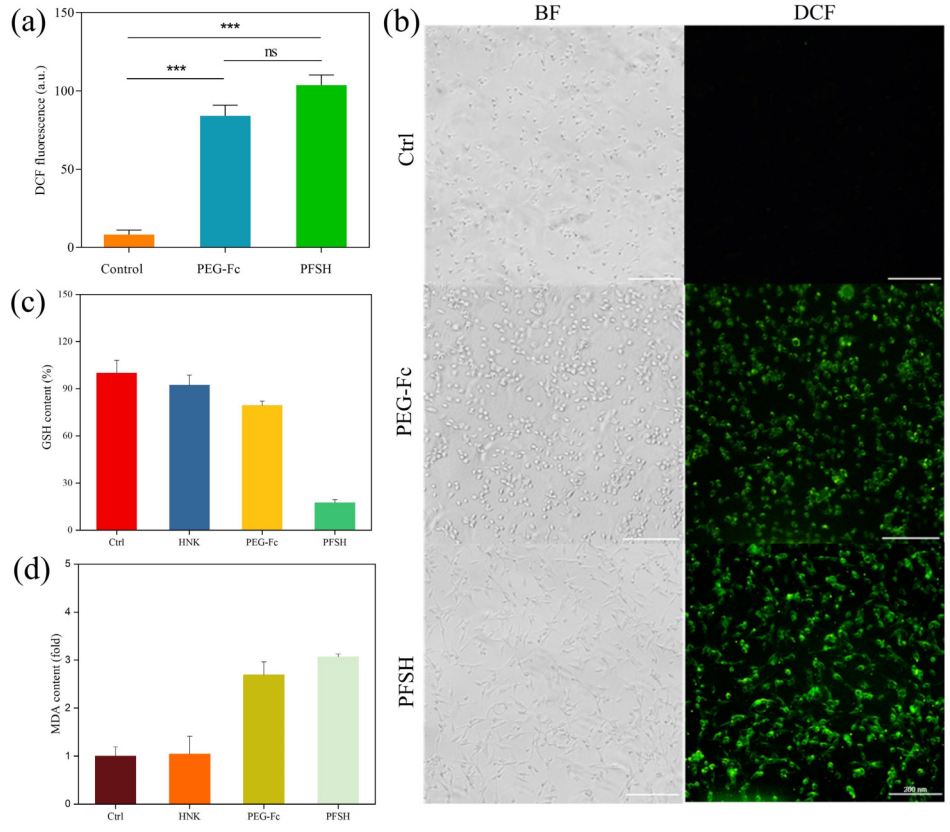

Figure 6 Intracellular ferroptosis efficacy of nano-prodrugs. (a) and (b) ROS imaging and quantification by DCFH-DA probe. (c) and (d) Relative GSH and MDA levels of CT26 cells incubated with different formulations. Scale bar: 200 μm.

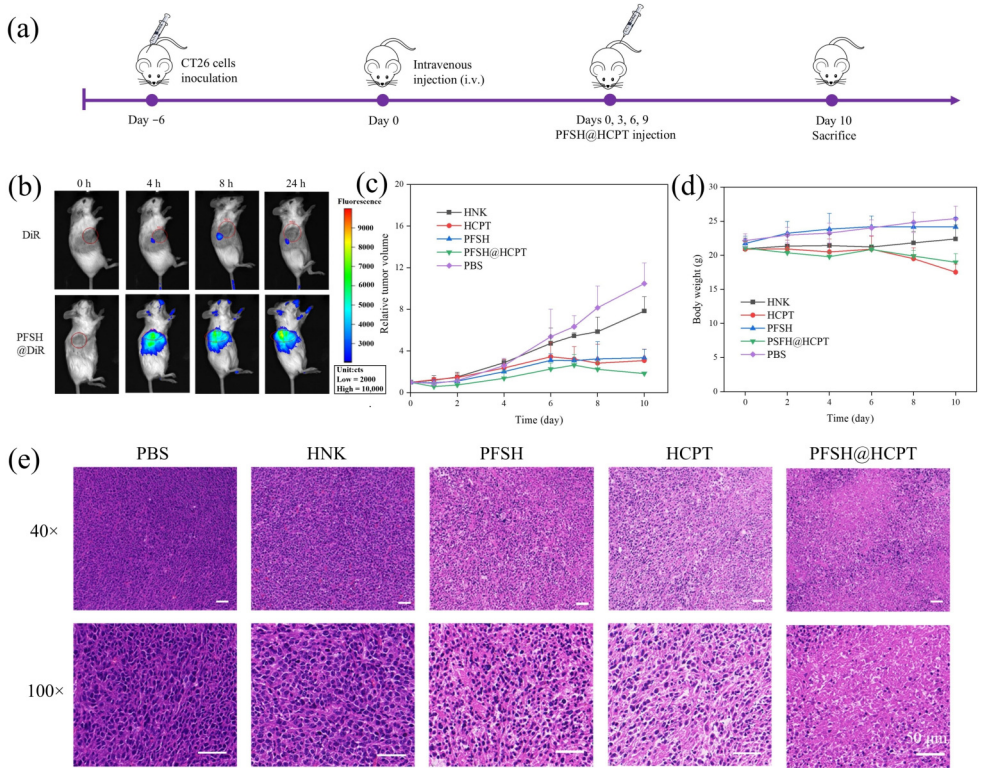

Figure 7 *In vivo* antitumor efficacy of nano prodrugs in CT26 tumor-bearing mice against different formulations (n = 5). (a) Schematic demonstration of mice tumor model establishment and treatment. (b) *In vivo* fluorescence images of tumor-bearing mice at different times after intravenous injection of DiR and PFSH@DiR. (c) Relative tumor volume changes during treatment. (d) Body weight changes during treatment. (e) H&E staining of tumor at the end of efficacy experiment. Scale bar: 50 μm.

4 Conclusion

Ferroptosis has emerged as a promising strategy for tumor treatment in combination with chemotherapy due to its ability to overcome chemotherapy-induced resistance. However, its action is still limited by high glutathione and ferroptosis inducer delivery efficiency. In this study, we successfully developed a self-assembled nano prodrug system to enhance the synergistic efficacy of ferroptosis and chemotherapy by co-delivery of disulfide bonds, HNK, Fc, and HCPT for the treatment of colon cancer. The nano prodrug system endowed the drug carriers with ferroptosis-inducing and chemotherapeutic efficacy and loaded with the chemotherapeutic agent, constructing a dual-mechanism induction of ferroptosis and a dual-mechanism reduction of drug resistance. The prodrug system showed good anti-tumor effects in a tumor-bearing mice model and no significant side effects were observed during treatment. This study realized the efficacy of "multi-mechanism", which may provide a new way for the treatment of colon cancer.

Electronic Supplementary Material: Supplementary material (synthetic route of PEG-Fc-SS-HNK (PFSH) copolymer; ^{1}H NMR spectra of NH_2-PEG-Fc, HNK-SS-COOH and PFSH; FT-IR spectra of NH_2-PEG-Fc, HNK-SS-COOH and PFSH; UV−Vis spectra of NH_2-PEG-Fc, HNK-SS-COOH and PFSH; mass spectra of HNK-SS-COOH and HNK-SH; hemolysis rate of the PFSH micelles and PFSH@HCPT micelles) is available in the online version of this article at https://doi.org/10.26599/NR.2025.94907298.

Date availability

All data needed to support the conclusions in the paper are presented in the manuscript and the ESM.

Acknowledgement

This study was supported by the Fundamental Research Funds for the Central Universities (No. PTYX202449).

Declaration of competing interest

All the contributing authors report no conflict of interests in this work.

Author contribution statement

L. M. Z.: Conceptualization, data curation, methodology, resources, software, investigation, formal analysis, project administration, writing – original draft, writing – review & editing. H. T. Z.: Data curation, methodology, resources, software, supervision, validation, writing – review & editing. Y. T. R.: Investigation, validation, writing – reviewing & editing. P. Y.: Investigation, validation, writing – review & editing. J. D. L.: Conceptualization, funding acquisition, resources, supervision, writing – review & editing.

Informed consent

Not applicable.

Ethics statement

All animal experiments were conducted in accordance with the relevant policies of the Experimental Animal Welfare and Ethics Committee of Beijing (KWT-2024-1022-03).

Use of AI statement

None.

References

[1] Tan, H. X.; Shen, Z. Q.; Wang, X. H.; Shu, S. C.; Deng, J.; Lu, L.; Fan, Z. Y.; Hu, D. N.; Cheng, P.; Cao, X. et al. Endoplasmic reticulum-targeted biomimetic nanoparticles induce apoptosis and ferroptosis by regulating endoplasmic reticulum function in colon cancer. *J. Control. Release* **2024**, *375*, 422–437.

[2] Wang, X.; Shao, G.; Hong, X. Y.; Shi, Y.; Zheng, Y. T.; Yu, Y. C.; Fu, C. Y. Targeting annexin A1 as a druggable player to enhance the anti-tumor role of honokiol in colon cancer through autophagic pathway. *Pharmaceuticals* **2023**, *16*, 70.

[3] Zhang, Z. T.; Ji, Y.; Hu, N.; Yu, Q. Q.; Zhang, X. R.; Li, J.; Wu, F. L.; Xu, H. E.; Tang, Q. Y.; Li, X. L. Ferroptosis-induced anticancer effect of resveratrol with a biomimetic Nano-delivery system in colorectal cancer treatment. *Asian J. Pharm. Sci.* **2022**, *17*, 751–766.

[4] Akakuru, O. U.; Zhang, Z. J.; Iqbal, M. Z.; Zhu, C. J.; Zhang, Y. W.; Wu, A. G. Chemotherapeutic nanomaterials in tumor boundary delineation: Prospects for effective tumor treatment. *Acta Pharm. Sin. B* **2022**, *12*, 2640–2657.

[5] Jin, H. J.; Wang, L. Q.; Bernards, R. Rational combinations of targeted cancer therapies: Background, advances and challenges. *Nat. Rev. Drug Discov.* **2023**, *22*, 213–234.

[6] Davodabadi, F.; Sajjadi, S. F.; Sarhadi, M.; Mirghasemi, S.; Nadali Hezaveh, M.; Khosravi, S.; Kamali Andani, M.; Cordani, M.; Basiri, M.; Ghavami, S. Cancer chemotherapy resistance: Mechanisms and recent breakthrough in targeted drug delivery. *Eur. J. Pharmacol.* **2023**, *958*, 176013.

[7] Pang, L.; Feng, H. H.; Zhong, W.; Dong, H. N.; Shen, Y. Q.; Yu, B.; Cong, H. L. Design of crown ether based micelles and their anti-tumor properties by perturbing potassium ion homeostasis. *Mater. Des.* **2021**, *211*, 110159.

[8] Zhang, C.; Liu, X. Y.; Jin, S. D.; Chen, Y.; Guo, R. H. Ferroptosis in cancer therapy: A novel approach to reversing drug resistance. *Mol. Cancer* **2022**, *21*, 47.

[9] Hangauer, M. J.; Viswanathan, V. S.; Ryan, M. J.; Bole, D.; Eaton, J. K.; Matov, A.; Galeas, J.; Dhruv, H. D.; Berens, M. E.; Schreiber, S. L. et al. Drug-tolerant persister cancer cells are vulnerable to GPX4 inhibition. *Nature* **2017**, *551*, 247–250.

[10] Chen, Y.; Yao, Z.; Liu, P. L.; Hu, Q. D.; Huang, Y.; Ping, L.; Zhang, F.; Tang, H. L.; Wan, T.; Ping, Y. et al. A self-assembly nano-prodrug for triple-negative breast cancer combined treatment by ferroptosis therapy and chemotherapy. *Acta Biomater.* **2023**, *159*, 275–288.

[11] Viswanathan, V. S.; Ryan, M. J.; Dhruv, H. D.; Gill, S.; Eichhoff, O. M.; Seashore-Ludlow, B.; Kaffenberger, S. D.; Eaton, J. K.; Shimada, K.; Aguirre, A. J. et al. Dependency of a therapy-resistant state of cancer cells on a lipid peroxidase pathway. *Nature* **2017**, *547*, 453–457.

[12] Yang, J.; Ma, S. Y.; Xu, R.; Wei, Y. W.; Zhang, J.; Zuo, T. T.; Wang, Z. H.; Deng, H. Z.; Yang, N.; Shen, Q. Smart biomimetic metal organic frameworks based on ROS-ferroptosis-glycolysis regulation for enhanced tumor chemo-immunotherapy. *J. Control. Release* **2021**, *334*, 21–33.

[13] Xu, R.; Yang, J.; Qian, Y.; Deng, H. Z.; Wang, Z. H.; Ma, S. Y.; Wei, Y. W.; Yang, N.; Shen, Q. Ferroptosis/pyroptosis dual-inductive combinational anti-cancer therapy achieved by transferrin decorated nanoMOF. *Nanoscale Horiz.* **2021**, *6*, 348–356.

[14] Li, J. S.; Zong, Q. Y.; Liu, Y.; Xiao, X.; Zhou, J. L.; Zhao, Z. Y.; Yuan, Y. Y. Self-catalyzed tumor ferroptosis based on ferrocene

conjugated reactive oxygen species generation and a responsive polymer. *Chem. Commun.* **2022**, *58*, 3294–3297.
[15] Gao, M.; Deng, J.; Liu, F.; Fan, A. P.; Wang, Y. J.; Wu, H. Y.; Ding, D.; Kong, D. L.; Wang, Z.; Peer, D. et al. Triggered ferroptotic polymer micelles for reversing multidrug resistance to chemotherapy. *Biomaterials* **2019**, *223*, 119486.
[16] Ren, Y. Q.; Mao, X. R.; Xu, H.; Dang, Q.; Weng, S. Y.; Zhang, Y. Y.; Chen, S.; Liu, S. T.; Ba, Y. H.; Zhou, Z. K. et al. Ferroptosis and EMT: Key targets for combating cancer progression and therapy resistance. *Cell. Mol. Life Sci.* **2023**, *80*, 263.
[17] Luo, J. J.; Li, Y.; Li, Y. R.; Chen, X. F.; Du, P. Y.; Wang, Z.; Tian, A. X.; Zhao, Y. J. Reversing ferroptosis resistance in breast cancer via tailored lipid and iron presentation. *ACS Nano* **2023**, *17*, 25257–25268.
[18] Hou, C. Y.; Yang, Y. M.; Wang, P. W.; Xie, H. M.; Jin, S. L.; Zhao, L. B.; Wu, G. H.; Xing, H.; Chen, H.; Liu, B. Y. et al. CCDC113 promotes colorectal cancer tumorigenesis and metastasis via TGF-β signaling pathway. *Cell Death Dis.* **2024**, *15*, 666.
[19] Gong, J.; Lin, Y. Y.; Zhang, H. Q.; Liu, C. Q.; Cheng, Z.; Yang, X. W.; Zhang, J. M.; Xiao, Y. Y.; Sang, N.; Qian, X. Y. et al. Reprogramming of lipid metabolism in cancer-associated fibroblasts potentiates migration of colorectal cancer cells. *Cell Death Dis.* **2020**, *11*, 267.
[20] Cai, M. R.; Fu, T. T.; Zhu, R. Y.; Hu, P. X.; Kong, J. H.; Liao, S. L.; Du, Y. J.; Zhang, Y. Q.; Qu, C. H.; Dong, X. et al. An iron-based metal-organic framework nanoplatform for enhanced ferroptosis and oridonin delivery as a comprehensive antitumor strategy. *Acta Pharm. Sin. B* **2024**, *14*, 4073–4086.
[21] Luo, S. W.; Ma, D.; Wei, R. L.; Yao, W.; Pang, X. R.; Wang, Y.; Xu, X. D; Wei, X. H.; Guo, Y.; Jiang, X. Q. et al. A tumor microenvironment responsive nanoplatform with oxidative stress amplification for effective MRI-based visual tumor ferroptosis. *Acta Biomater* **2022**, *138*, 518–527.
[22] Yang, Y. X.; Zuo, S. Y.; Li, L. X.; Kuang, X.; Li, J. B.; Sun, B. J.; Wang, S. J.; He, Z. G.; Sun, J. Iron-doxorubicin prodrug loaded liposome nanogenerator programs multimodal ferroptosis for efficient cancer therapy. *Asian J. Pharm. Sci.* **2021**, *16*, 784–793.
[23] Liu, J. P.; Zhan, J. Z.; Zhang, Y.; Huang, L.; Yang, J.; Feng, J.; Ding, L. W.; Shen, Z. Y.; Chen, X. Y. Ultrathin clay nanoparticles-mediated mutual reinforcement of ferroptosis and cancer immunotherapy. *Adv. Mater.* **2024**, *36*, e2309562.
[24] Han, Y. K.; Dong, Z. L.; Wang, C. J.; Li, Q. G.; Hao, Y.; Yang, Z. J.; Zhu, W. J.; Zhang, Y. Y.; Liu, Z.; Feng, L. Z. Ferrous ions doped calcium carbonate nanoparticles potentiate chemotherapy by inducing ferroptosis. *J. Control. Release* **2022**, *348*, 346–356.
[25] Zhang, Y. R.; Song, Q. C.; Zhang, Y. Y.; Xiao, J. H.; Deng, X. T.; Xing, X.; Hu, H. Z.; Zhang, Y. Z. Iron-based nanovehicle delivering fin56 for hyperthermia-boosted ferroptosis therapy against osteosarcoma. *Int. J. Nanomedicine* **2024**, *19*, 91–107.
[26] Xin, H.; Yuan, P. J.; Wang, Y. J.; Xiao, J. M.; Tian, G.; Fan, Y.; Zhang, G. L.; Liu, L. Highly selective and effective ferroptosis liposomal nanodrugs for synergistic antitumor therapy. *Chem. Eng. J.* **2024**, *493*, 152480.
[27] Huang, Y.; Lin, Y.; Li, B. W.; Zhang, F.; Zhan, C. Y.; Xie, X.; Yao, Z.; Wu, C. Z.; Ping, Y.; Shen, J. L. Combination therapy to overcome ferroptosis resistance by biomimetic self-assembly Nano-prodrug. *Asian J. Pharm. Sci.* **2023**, *18*, 100844.
[28] Wang, W. J.; Ling, Y. Y.; Zhong, Y. M.; Li, Z. Y.; Tan, C. P.; Mao, Z. W. Ferroptosis-enhanced cancer immunity by a ferrocene-appended iridium(III) diphosphine complex. *Angew. Chem., Int. Ed.* **2022**, *61*, e202115247.
[29] Gao, Y. C.; Zhang, H. C.; Tang, L.; Li, F. F.; Yang, L.; Xiao, H. H.; Karges, J.; Huang, W. H.; Zhang, W.; Liu, C. Y. Cancer nanobombs delivering artoxplatin with a polyigniter bearing hydrophobic ferrocene units upregulate PD-L1 expression and stimulate stronger anticancer immunity. *Adv. Sci.* **2024**, *11*, e2300806.
[30] Guo, C.; Liu, P.; Deng, G. L.; Han, Y.; Chen, Y. H.; Cai, C. J.; Shen, H.; Deng, G. P.; Zeng, S. Honokiol induces ferroptosis in colon cancer cells by regulating GPX4 activity. *Am. J. Cancer Res.* **2021**, *11*, 3039–3054.
[31] Wang, Z. Q.; Li, X. R.; Wang, D. S.; Zou, Y.; Qu, X. Y.; He, C. Y.; Deng, Y. Q.; Jin, Y.; Zhou, Y. H.; Zhou, Y. X. et al. Concurrently suppressing multidrug resistance and metastasis of breast cancer by co-delivery of paclitaxel and honokiol with pH-sensitive polymeric micelles. *Acta Biomater.* **2017**, *62*, 144–156.
[32] Xu, D.; Lu, Q. H.; Hu, X. Down-regulation of P-glycoprotein expression in MDR breast cancer cell MCF-7/ADR by honokiol. *Cancer Lett.* **2006**, *243*, 274–280.
[33] Dai, S. Y.; Qin, W. X.; Yu, S.; Li, C.; Yang, Y. H.; Pei, Y. H. Honokiol and magnolol: A review of structure-activity relationships of their derivatives. *Phytochemistry* **2024**, *223*, 114132.
[34] Le, D. T. T.; Nguyen, N. H.; Do, H. T. M.; Vu, C. M.; Nguyen, P. T. M.; Chu, H. H. Honokiol-loaded PLGA-PEG nanoparticles with solubility in water for infusion treatment of solid cancer. *J. Drug Deliv. Sci. Technol.* **2025**, *103*, 106436.
[35] Yang, B.; Gao, J.; Pei, Q.; Xu, H. X.; Yu, H. J. Engineering prodrug nanomedicine for cancer immunotherapy. *Adv. Sci.* **2020**, *7*, 2002365.
[36] Zhou, S.; Zhong, Q.; Wang, Y.; Hu, P.; Zhong, W.; Huang, C. B.; Yu, Z. Q.; Ding, C. D.; Liu, H. X.; Fu, J. J. Chemically engineered mesoporous silica nanoparticles-based intelligent delivery systems for theranostic applications in multiple cancerous/non-cancerous diseases. *Coord. Chem. Rev.* **2022**, *452*, 214309.
[37] Li, Y. R.; Feng, S. M.; Dai, P. P.; Liu, F.; Shang, Y. Q.; Yang, Q.; Qin, J.; Yuchi, Z.; Wang, Z.; Zhao, Y. J. Tailored Trojan horse nanocarriers for enhanced redox-responsive drug delivery. *J. Control. Release* **2022**, *342*, 201–209.
[38] Yao, W. H.; Liu, C. Y.; Wang, N.; Zhou, H. J.; Chen, H. L.; Qiao, W. H. An MRI-guided targeting dual-responsive drug delivery system for liver cancer therapy. *J. Colloid Interface Sci.* **2021**, *603*, 783–798.
[39] Cheng, R.; Meng, F. H.; Deng, C.; Zhong, Z. Y. Bioresponsive polymeric nanotherapeutics for targeted cancer chemotherapy. *Nano Today* **2015**, *10*, 656–670.
[40] Chen, J. J.; Song, Y. R.; Yang, W. Q.; Guo, J. H.; Zhang, S. H.; Wan, D.; Liu, Y. H.; Pan, J. Enzyme and reduction dual-responsive peptide micelles as nanocarriers for smart drug delivery. *ACS Appl. Nano Mater.* **2023**, *6*, 16179–16188.
[41] Li, B. L.; Teng, J. K.; Chen, S.; Yang, J. M.; Liu, X. Q.; Zhang, J.; Zhao, Y. A dual‐stimuli responsive supramolecular nanovector anchoring folic acid ligands for targeted delivery of anti‐colorectal drug hydroxycamptothecin. *J. Appl. Polym. Sci.* **2023**, *140*, e53525.